## RESEARCH ARTICLE

Check for updates

# Photostable rubyrins bearing pentafluorophenyl pendants for enhanced reactive oxygen species generation using an 808 nm laser

Aathira Edwin, Thondikkal Sulfikarali,† Gowtham Raj,† Athira Naniyil, Reji Varghese [ID] and Sabapathi Gokulnath [ID] *

Organic photosensitizers with long-wavelength absorption, photostability and tumour specificity are highly desired in photodynamic therapy (PDT), but the molecular design for this three-in-one formula is quite challenging. Herein, we report the molecular engineering of a series of expanded porphyrinoids with *N*-anisyl dithienopyrrole (DTP) and *meso*-pentafluorophenyl substituents to collectively accelerate the reactive oxygen species (ROS) generation. Due to extensive π-conjugation, the Q-bands are significantly red-shifted, extending into the near-IR region. Hence, this series of molecules can be photoactivated using the deeply penetrating 808 nm laser. Interestingly, subtle tuning of singlet oxygen production could be achieved by increasing the number of *meso*-pentafluorophenyl pendants. This was corroborated *via* photophysical and theoretical studies, which suggested altered electron distribution and stabilization of energy levels for rubyrins with four pentafluorophenyl substituents. On the contrary, heptaphyrin with its increased π-electrons exhibited no ROS generation due to the mismatch in energy gap with molecular oxygen. The photodynamic properties of these macrocycles and their respective nanoparticles, including their remarkable ROS generation, exceptional photostability and biocompatibility, demonstrate their potential as excellent candidates for PDT. The *in vitro* experiments substantiate the effective anticancer activity of these nanoparticles, offering future potential opportunities for application *via in vivo* PDT and bioimaging.

## Introduction

Photodynamic therapy (PDT) is an emerging field in cancer research that is used to destroy malignant cells *via* a non-invasive protocol. It involves a photosensitizer (PS), which goes to the excited singlet state upon irradiation with a suitable wavelength. From there, the triplet state is populated *via* intersystem crossing (ISC) and will generate $^1O_2$ or reactive oxygen species (ROS) upon interaction with molecular oxygen.[1] Such species are transient, highly cytotoxic, and can induce cell death and vascular shutdown, eventually leading to tumour destruction.[2] In the ever-growing library of photosensitizers, organic near-infrared (NIR) fluorophores are quite special due to their ease of functionalization, biocompatibility, low dark toxicity and easy metabolism.[3] Among them, porphyrins stand out as excellent PSs for PDT[4] due to their high molar extinction coefficients, broad absorption range, high quantum yield of the

triplet state, superior photostability and more importantly, their unique affinity towards tumour tissues.[5] Therefore, from the first clinically authorized PS for PDT (Photofrin®, a hematoporphyrin derivative), the demand for porphyrin-based systems has been steadily increasing.[4]

While regular tetrapyrrolic, peripherally extended and core-modified porphyrins have been extensively studied for various phototherapeutic modalities,[6] research on expanded porphyrins is still in its infancy. Expanded porphyrins are promising candidates in phototheranostics due to their remarkably low HOMO–LUMO gap, which shifts their optical bands into the NIR-I, II and III regions. Such pigments with extensive π-conjugation provide a scope for utilizing NIR-light with maximum tissue penetration and minimal scattering. Examples include five-membered expanded porphyrins, such as texaphyrins and sapphyrins, which have been studied for tumour localization, MRI, and PDT and have even progressed up to clinical trials.[7] However, biomedical applications of hexaphyrins have been less explored. It was a decade ago that Tian *et al.* reported the first rubyrin showing PDT activity. The cell-specific and pH-activatable nanoparticles of this phenanthrene-fused rubyrin could efficiently generate ROS in cancer tissues upon irradiation with 635 and

*School of Chemistry, Indian Institute of Science Education and Research, Thiruvananthapuram-695551Maruthamala P.O., Vithura, Kerala, India. E-mail: gokul@iisertvm.ac.in*

† These authors contributed equally to this work.

808 nm lasers.[8] The design strategy involved the use of a dimethyl amino moiety at the *meso*-position, which offered pH-controllable activity and enhanced selectivity towards cancer cells. Although a few hexaphyrins have been reported for photoacoustic imaging and photothermal therapy,[9] this phenanthrene-fused rubyrin remains the only hexaphyrin showing promise for PDT. Thus, further investigations into expanded π-systems with coveted NIR properties and superior stability are being actively pursued.[10]

Designing PSs that are free of heavy atoms without compromising their ISC properties is often challenging.[11] However, the introduction of fluorine atoms into porphyrin derivatives is known to reduce electron density as compared to nonfluorinated derivatives, which may improve intersystem crossing, the triplet quantum yield, and hence, the ROS production.[12] Fluorine has high electronegativity and ionization energy. Furthermore, its perfluorinated forms (like $-CF_3$, $-C_6F_5$ and $-OCF_3$) can impart significant steric bulk, alter the HOMO–LUMO energy levels, prevent photooxidation and even improve pharmacokinetics. Since perfluorocarbons are known to bind and release oxygen to mitigate hypoxia,[13] the incorporation of pentafluorophenyl pendants into the porphyrinoid framework could enhance oxygen solubility and boost ROS production. The same pentafluorophenyl group can also serve as an endoplasmic reticulum targeting moiety. Hence, the tumour-specificity of porphyrins could be enhanced.[14]

In this work, we describe the synthesis, characterization and ROS generation capabilities of a series of novel dithienopyrrole-based rubyrins and heptaphyrin. These porphyrinoids were incorporated with varying numbers of *meso*-pentafluorophenyl units to understand their role in determining the photostability, oxygen affinity, alteration of energy levels, and photosensitization ability. They were also embedded with sulphur atoms and electron-donating DTP with methoxy units, both of which are known to boost ROS generation.[15] We also demonstrate the successful nanoencapsulation of these bulky, hydrophobic macrocycles into water-soluble constructs using DSPE:mPEG$_{2000}$, an amphiphilic polymer. Such FDA-approved PEG-based carriers are known to have long circulation times, mucus-penetrating abilities and high encapsulation efficiency.[16] The photodynamic response of these macrocycles was exploited using an 808 nm continuous laser, and the *in vitro* experiments were performed in MDA-MB-231 cells.

## Results and discussion

We have designed a series of DTP-embedded 26π rubyrins **1**, **2a**, **2b**, and a further expanded analogue, 30π heptaphyrin **3**, with varying *meso* substituents. The structural design was such that the role of pentafluorophenyl moieties in enhancing ROS generation could be studied in detail. For this, we started our synthesis from a rigid DTP-based tetrapyrrane **4**, which was previously reported by our research group.[17] The condensation of **4** with the related DTP dicarbinol **5** in the presence of *para*-toluenesulfonic acid (*p*-TSOH), followed by *para*-chloranil mediated oxidation, provided the highly symmetric doubly fused rubyrin **1** in 23% yield (Scheme 1). Similarly, the singly
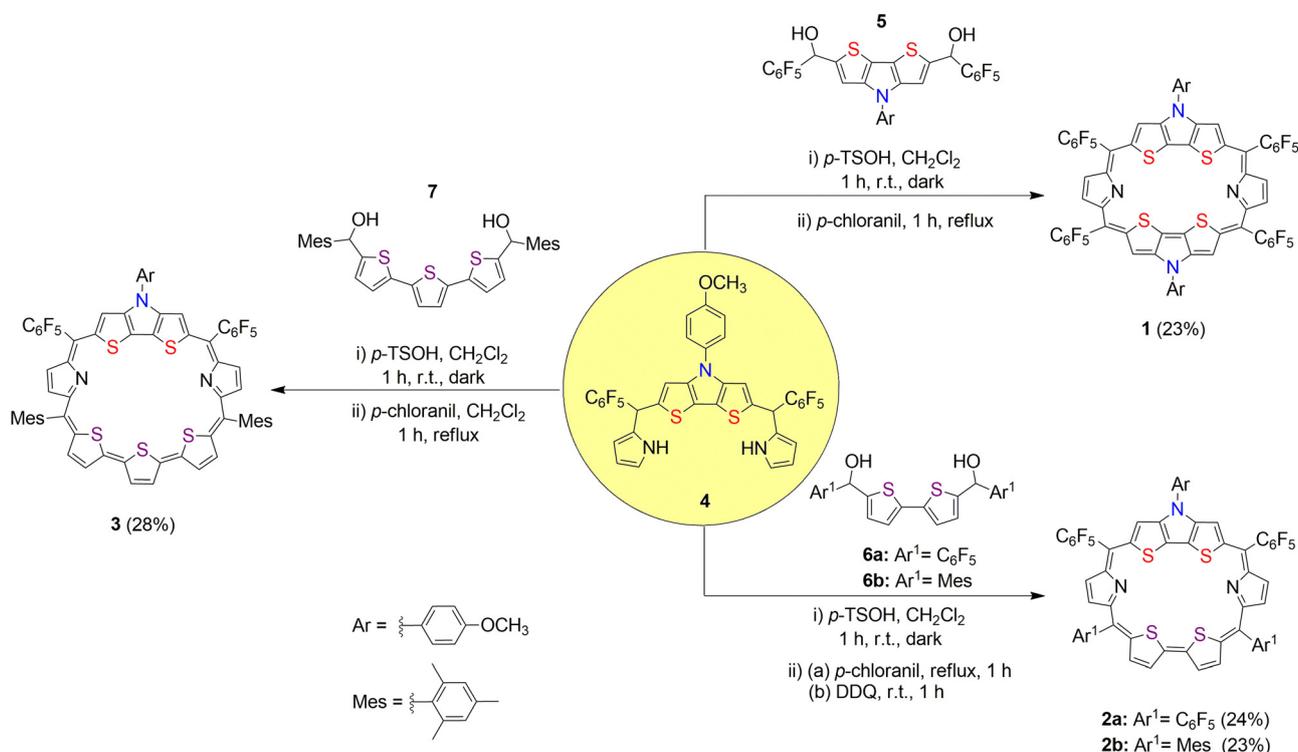


**Scheme 1** Synthesis of macrocycles **1**, **2a**, **2b** and **3**.

fused rubyrins **2a** and **2b** were also obtained in good yields by utilizing bithiophene diols bearing different *meso* substituents. Subsequently, heptaphyrin was also prepared by condensing **4** with terthiophene diol **7** to afford **3** as purple solids in 28% yield. These macrocycles were stable for several months at room temperature and stable enough during silica/alumina column chromatography. Moreover, they exhibited good solubility in a range of organic solvents because of the introduction of *p*-anisyl unit(s).[18] HR-MS analysis supported the formation of **1**, **2a**, **2b** and **3**, which showed parent peaks at *m/z* of 1411.0425 $[M + H]^+$, 1290.9938 $[M]^+$, 1196.1877 $[M + H]^+$ and 1278.1769 $[M + H]^+$ respectively (Fig. S3-1–S3-4).

To understand the solution state structure of these macrocycles, $^1H$ NMR spectra were recorded in CDCl$_3$ at 298 K. For rubyrin **1**, β-protons of DTP (**d**) and pyrrole (**e**) subunits appeared as sharp singlets at 10.45 and 9.49 ppm, respectively. The proton **d** was spatially coupled with the phenyl proton **c**, and the methoxy protons showed spatial correlation with protons **b**, as indicated in the $^1H$–$^1H$ ROESY spectrum (Fig. S4-3). Conversely, the singly fused rubyrin **2a** revealed a less symmetric $^1H$-NMR spectral pattern, with the β-pyrrolic protons splitting into two closely placed doublets at 9.35 and 9.29 ppm, respectively (Fig. S4-4). For the mesityl derivative **2b**, the spatial correlation between the mesityl proton **j** and the adjacent pyrrolic proton **f** aided in the assignment of the individual β-pyrrolic protons (Fig. S4-9). The structure of heptaphyrin **3** could also be deduced in a similar manner, combining $^1H$, COSY and ROESY spectroscopic techniques (Fig. S4-10–S4-12). The central thiophene protons of the terthiophene subunit **i** exhibited a singlet at 11.20 ppm, whereas the signals corresponding to β-pyrrolic proton **e** and phenyl proton **c** merged into a multiplet at around 8.5 ppm, supporting the merged correlation seen in the COSY spectrum (Fig. S4-11).

X-ray quality single crystals of **1** were obtained by vapour diffusion of acetone into a chloroform solution of **1** at room temperature. The crystal data revealed a dome-shaped structure, stabilized by two S···N interactions at a distance of 2.73 Å and 2.64 Å, respectively (Fig. 1). The absence of inverted heterocycles confirms the rigidity of the system, and the heteroatoms experienced minimal deviation in the range of 0.135–0.293 Å from the mean macrocyclic plane (defined by four *meso*-carbons). The tilt angle from the mean plane for two DTP subunits were 10.09° and 17.29°, which is larger than that of the planar DTP-based octaphyrin (0.39°).[17] Both *N*-anisyl (*ca.* 66° and 73°) and four *meso*-pentafluorophenyl substituents aligned in a non-coplanar fashion to avoid steric congestion between the β-CHs of the neighbouring heterocycles.

Crystal packing analysis revealed several interactions originating from the electronegative atoms, electron-rich π-units, and crystalized solvents. A strong C–H···O intermolecular hydrogen bonding interaction was found (2.546 Å, 170.16° and 2.642 Å, 164.79°) between the β-hydrogen of DTP and methoxy oxygen of the adjacent molecule, which propagated along the *b*-axis (Fig. S5-2). Innumerable C–H···F and C–F···π interactions were found throughout the three-dimensional network due to the presence of multiple pentafluorophenyl
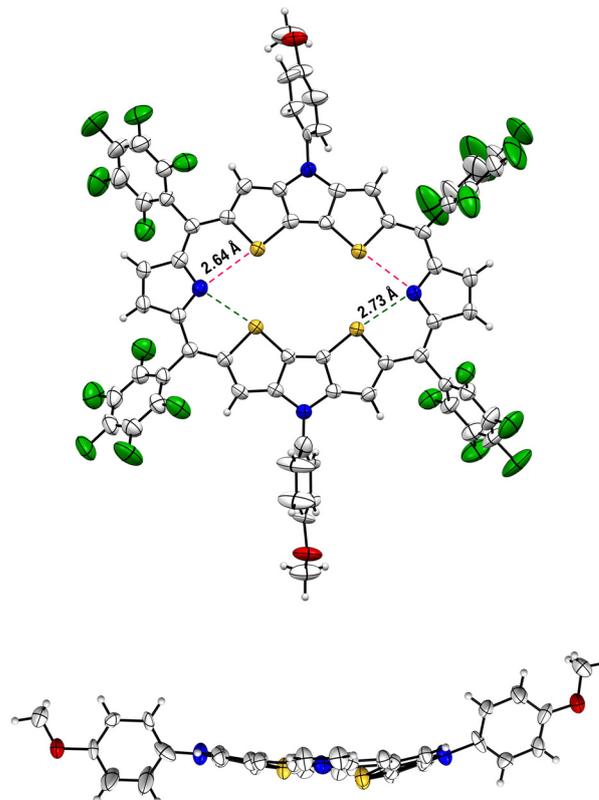


**Fig. 1** Single crystal X-ray structure of **1**. Bond lengths pertaining to S···N interactions are shown. Meso-pentafluorophenyl substituents are omitted for clarity in the side view.

substituents. A notable C–H···F intermolecular interaction (2.546 Å, 147.5° and 2.655 Å, 139.46°) appeared between the β-hydrogen of pyrrole and *para*-fluorine of the C$_6$F$_5$ unit (Fig. S5-3).

The UV-vis-NIR absorption spectra of the macrocycles recorded in dichloromethane correlated with that of the aromatic expanded porphyrinoids, extending to the NIR-I region (Fig. 2).[19] The rubyrins have large molar extinction coefficients, where **1** exhibited a sharp Soret band at 528 nm $[\varepsilon = 4.5 \times 10^5 \text{ M}^{-1} \text{ cm}^{-1}]$ and three Q-bands at 680, 734 and 777 nm. Upon protonation using trifluoroacetic acid, the Soret band shifted to 540 nm with a shoulder feature, and the broad Q-bands ranged from 670 to 920 nm. Rubyrin **2a** displayed a Soret band at 527 nm $[\varepsilon = 4.26 \times 10^5 \text{ M}^{-1} \text{ cm}^{-1}]$ and three well-defined Q-bands at 671, 723 and 798 nm. The mesityl derivatives **2b** also showed absorption features that were similar to those of **2a**, although **2a·2H$^+$** manifested a split Soret band at 533 and 582 nm. Conversely, the expanded analogue, heptaphyrin **3**, revealed a relatively bathochromic-shifted absorption that extended up to 1000 nm, owing to the increased π-electrons in the aromatic circuit. The Soret bands with split characteristics appeared at 554 nm $[\varepsilon = 2.43 \times 10^5 \text{ M}^{-1} \text{ cm}^{-1}]$ and 586 nm, followed by four Q-bands at 730, 798, 920 and 967 nm. A vivid colour change from violet to a deep blue and the intensification of the absorption bands were observed upon protonation. This is likely due to the effective π-conjugation in **3·2H$^+$**. The protonated form
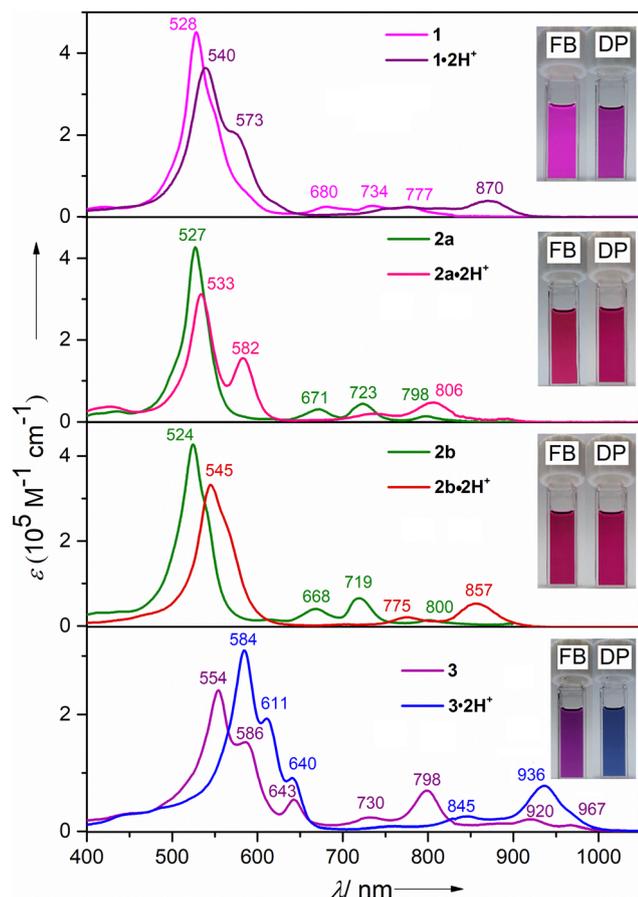
**Fig. 2** UV-vis-NIR absorption spectra of the macrocycles and their corresponding protonated forms, recorded in $CH_2Cl_2$. Inset shows the respective colours of the macrocycles (FB = freebase and DP = diprotonated).

manifested Soret-like features at 584, 611 and 640 nm, accompanied by Q-bands at 845 and 936 nm. The emission spectral data revealed that all four macrocycles exhibit weak fluorescence and Stokes shift in the range $\Delta\lambda = 50$–250 nm with emission maxima reaching the NIR-II window (*ca.* 1069 to 1189 nm) (Fig. S6-1). Such NIR-emissive substrates show promise for applications in optical communication, bioimaging, lasers, organic light-emitting diodes (OLEDs), military technology, *etc.*[20]

To understand the redox properties of these macrocycles, cyclic voltammograms and differential pulse voltammograms were recorded in dichloromethane using tetrabutylammonium hexafluorophosphate (TBAPF$_6$) as a supporting electrolyte. The rubyrins exhibited two reversible oxidation waves, one reversible ($E_{red1}$) and one quasi-reversible reduction wave ($E_{red2}$). Meanwhile, the heptaphyrin **3** displayed two oxidation and two reduction processes, with both being highly reversible in nature (Fig. S7-1). For macrocycle **1**, the peaks were observed at $E_{ox1} = 0.45$ V, $E_{ox2} = 0.67$ V, $E_{red1} = -0.95$ V and $E_{red2} = -1.23$ V. The singly fused analogue **2a** exhibited more positive oxidation potentials ($E_{ox1} = 0.55$ V, $E_{ox2} = 0.94$ V, $E_{red1} = -0.91$ V and $E_{red2} = -1.20$ V) compared to **1**, which suggests the electron-richness of the doubly fused congener **1**. As expected, **2b** was easier to oxidise and more difficult to reduce when compared to

**2a** due to the electron-donating mesityl groups in **2b** ($E_{ox1} = 0.37$ V, $E_{ox2} = 0.75$ V, $E_{red1} = -1.10$ V and $E_{red2} = -1.42$ V). For heptaphyrin **3**, relatively easier oxidations were observed at $E_{ox1} = 0.23$ V and $E_{ox2} = 0.58$ V, along with reductions at $E_{red1} = -1.03$ V and $E_{red2} = -1.29$ V, all of them being reversible in nature. The reduction in the electrochemical HOMO–LUMO gap for **3** (1.26 eV) is due to its larger π-system when compared to **1** (1.40 eV), **2a** (1.46 eV), and **2b** (1.47 eV).

To gain theoretical insights, DFT calculations were done at B3LYP/6-31G(d,p) level of theory. The optimised geometry of **1** resembled that of its X-ray crystallographic structure, with a dome-type conformation (Fig. S9-1). Other macrocycles revealed a perfect planar conformation from the respective optimised structures, with significant distortions for their protonated forms (Fig. S9-2–S9-4). Analysis of the frontier molecular orbitals suggested that the electron density is well-distributed over the entire π-circuit, which confirmed the global annulenic conjugation (Fig. S9-6–S9-9). The near degeneracy of H−1/H and L/L+1 is consistent with the aromaticity predicted by the Gouterman four orbital model (HOMO: H and LUMO: L).[21] The theoretical band gaps of **1**, **2a**, **2b** and **3** were calculated to be 1.97, 1.97, 1.95 and 1.67 eV, respectively (Fig. S9-5). In contrast to the mesityl-substituted macrocycles, the all-pentafluorophenyl substituted derivatives **1** and **2a** possess strongly stabilised energy levels. Notably, the protonated forms showed a reduced HOMO–LUMO gap due to non-planar deformations arising upon protonation.[22] This is in agreement with the red-shifted absorption spectra obtained for the protonated species. The vertical excitations predicted by TD-DFT calculations were found to correlate well with the absorption spectral bands typical for aromatic porphyrinoids. The AICD plots depicted a global conjugation with ring current vectors moving clockwise in both freebase and protonated forms, suggesting the strong diatropic ring current (Fig. S9-14–S9-17). Furthermore, the extent of aromaticity was quantified using NICS(0) values (**1**: −14.80 ppm, **2a**: −14.78 ppm, **2b**: −14.24 ppm, **3**: −13.50 ppm) (Fig. S9-10–S9-13). The enhanced aromaticity of thiophene rings (*ca.* −20 ppm) when compared to the free thiophene (−13.3 ppm) is exclusively due to the global diatropic ring current.

Due to the NIR absorption of these macrocycles (*ca.* 800 nm), their photodynamic properties were investigated using an 808 nm laser (1 W cm$^{-2}$, unless mentioned otherwise). Such a wavelength is known to have excellent tissue penetration properties, precise targeting, minimal absorption by endogenous chromophores and minimal collateral damage.[23] Fortunately, no deterioration of absorption peaks was observed upon laser exposure (808 nm, 1 W cm$^{-2}$) for over 30 min in DMF, confirming their good photostability in polar media (Fig. S8-1 and Fig. 3(a)). ROS generation studies were done using 1,3-diphenyl-isobenzofuran (DPBF) as the ROS scavenger. When these macrocycles with excess DPBF were irradiated with the 808-nm laser, rapid degradation of the DPBF peak at 415 nm was observed within a few seconds (Fig. S8-2). This result suggests that **1** and **2a** are excellent ROS generators and could potentially be used in PDT. Although **2b** also produced ROS, the
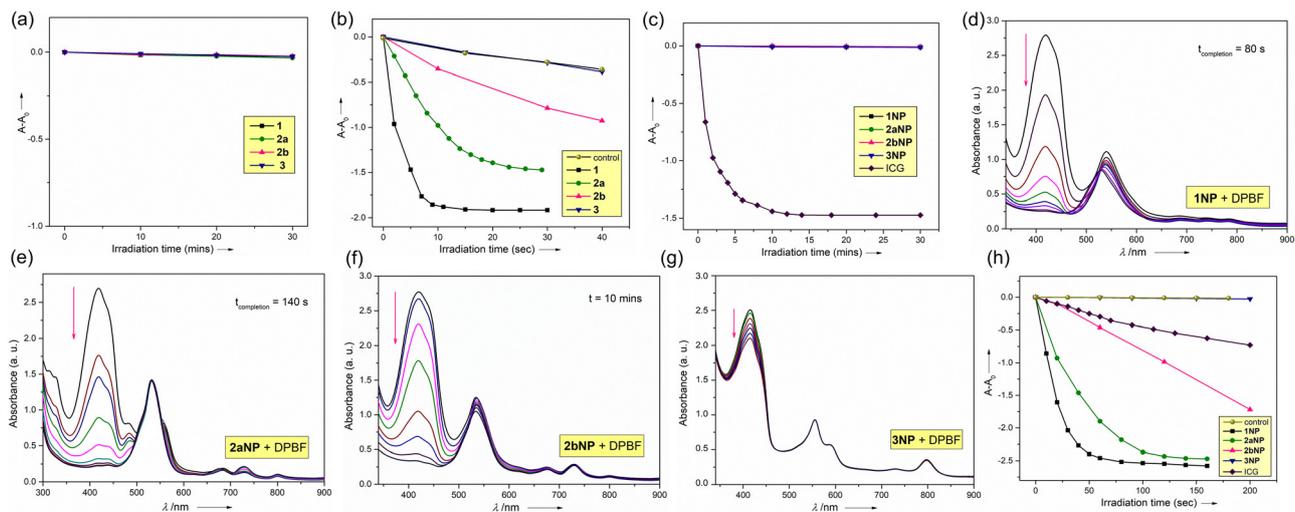
**Fig. 3** Change in absorbance with respect to laser irradiation time for (a) DMF solutions of macrocycles and (c) aqueous solutions of nanoparticles and ICG. Time-dependent DPBF degradation for (b) DMF solutions of macrocycles and (h) aqueous solutions of nanoparticles and ICG upon laser illumination. Figures (d) to (g) depict the time-dependent absorption spectral changes of DPBF when treated with NPs and exposed to NIR light. All of these experiments were conducted using an 808 nm laser at 1 W cm$^{-2}$.

rate was lower than that of the other rubyrins with increased pentafluorophenyl substituents. Among the four substrates under study, heptaphyrin **3** exhibited no ROS generation. This is probably due to the mismatch of energy levels with that of $O_2$, which is evident from the zero–zero excitation energy obtained from the intersection point of their normalized absorption and emission spectra.[9] The $E_{0-0}$ values for **1**, **2a**, **2b** and **3** were calculated to be 1.40, 1.41, 1.43 and 1.25 eV, respectively. Since the $S_1$ energy level for **3** is low, its $T_1$ energy level would be even lower, probably close to that of singlet oxygen (0.98 eV), which hampers the effective ROS production. Hence, it can be concluded that **1** and **2a** exhibit remarkable activity because of the increased number of perfluorophenyl groups, which leads to a substantial rise in the oxygen affinity. This, in turn, boosts their ROS production despite having a similar $S_1$ level to **2b**.

Considering the excellent photostability and ROS generation capacity of these macrocycles, they were nano-encapsulated using a phospholipid polymer, namely DSPE: mPEG$_{2000}$, to make biocompatible constructs for *in vitro* studies. The nanoparticles (NPs) were prepared using the conventional sonication method, and the encapsulation efficiencies for **1NP**, **2aNP**, **2bNP**, and **3NP** were calculated to be 95%, 98%, 99%, and 88% respectively.[24] Notably, the absorption characteristics remain unaltered even after nanoencapsulation, with the retention of Q-bands at around 800 nm (Fig. S8-3). This suggests the monomeric character of these macrocycles in aqueous formulation. Hence, their ROS generation studies were performed using the same laser. Initially, the photostability of the nanoparticles was assessed and compared with commercial dye ICG. The NPs showed remarkable photostability and did not undergo any degradation when illuminated for over 30 min (Fig. S8-4). Conversely, ICG underwent gradual degradation over the course of irradiation for 10 min (Fig. 3(c)). The NPs were found to be stable for more than 60 days when stored at

4 °C in the dark. For the ROS generation study on NPs, a molar excess solution of DPBF was mixed with the respective NPs and irradiated using the 808-nm laser. Similar to **1** and **2a**, their aqueous formulations **1NP** and **2aNP** also exhibited excellent ROS generation capacity, affirming their potential as efficient photosensitizers for PDT with the 808 nm NIR laser (Fig. 3(e) and (f)). However, the response slightly declined in water due to the low solubility of oxygen in water when compared to organic solvents (Fig. 3(g)).[25] While the activity of **2bNP** was lower, **3NP** showed the lowest ROS generation (similar to the control study), confirming that it is not an ideal candidate for PDT (Fig. 3(h)). Fig. 4(d) depicts the comparison of the ROS generation capacities of various NPs along with ICG. It is clear that **1NP** and **2aNP** are excellent photosensitizers and may be used for *in vitro* studies. To rule out other possible pathways, such as photothermal activity, the temperature responses of the nanoparticles were monitored by irradiation with the 808 nm laser. No significant enhancement in temperature was observed, suggesting that these photosensitizers operate solely *via* the PDT pathway (Fig. S8-5b).

Considering the superior properties, **1NP** and **2aNP** were used for *in vitro* studies with MDA-MB-231 cells. The ROS generation of these nanoparticles was analyzed using the 2′,7′-dichlorofluorescein diacetate (DCFH-DA) assay, where DCFH-DA is a redox-responsive probe that furnishes a highly fluorescent DCF in the presence of ROS.[26] For this study, after 3 h of incubation, the NP-treated MDA-MB-231 cells were irradiated with the 808 nm laser (1.5 W cm$^{-2}$) for 10 min. Due to *in situ* ROS generation inside the cell, the green fluorescence of 2,7-dichlorofluorescein (DCF) was observed upon ROS detection, as monitored using confocal laser scanning microscopic imaging (CLSM) (Fig. 4(a) and (b)). The CLSM analyses clearly revealed the maximum green fluorescence intensity of DCF for the NP-treated cells after NIR light illumination,
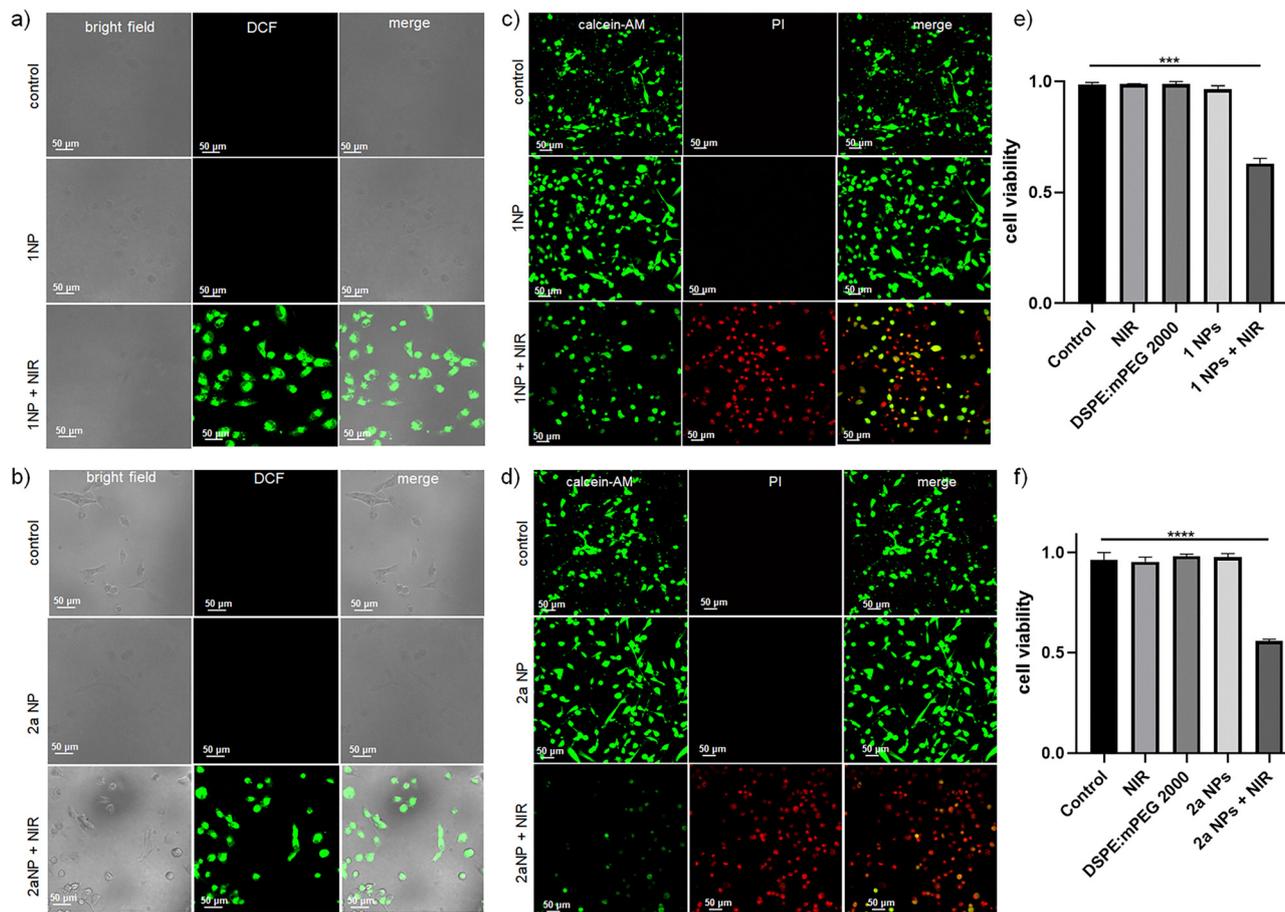
**Fig. 4** CLSM images comparing the $^1O_2$ generation capability of (a) **1NP** and (b) **2aNP**-treated MDA-MB-231 cells using the DCFH–DA assay. Calcein-AM/PI live−dead cell assay of (c) **1NP** and (d) **2aNP**-treated MDA-MB-231 cells. An MTT assay demonstrating the cytotoxicity of (e) **1NP** and (f) **2aNP**. Statistical significance was calculated using GraphPad software with the two-tailed Student's $t$-test to compare the cell viability in different treatment groups with the control (*$p < 0.05$; **$p < 0.01$, ***$p < 0.001$, and ****$p < 0.0001$). [NP] = 40 μM.

which is in sharp contrast to that of the untreated cells and NPs alone in the absence of NIR light. This confirms that the **1NP** and **2aNP**-treated cells produce ROS inside the cells only upon NIR light illumination.

We further studied the toxicity of the nanoparticles in MDA-MB-231 cells using the live/dead cell assay. Calcein-AM can interact with the esterase present inside the live cancer cells and produce green fluorescence from the cells due to the cleavage of the acetoxymethyl (AM) ester-protecting group of calcein-AM. In contrast, no ester cleavage is possible inside the dead cells, as the concentration of esterase is very low. Hence, no green fluorescence is expected for the dead cells. Similarly, propidium iodide (PI) cannot pass through the cell membrane of live cells. In contrast, it can stain dead cells to give red fluorescence.[27] To perform the live/dead assay, cells were initially treated with **1NP** and **2aNP** for 3 h, followed by irradiation with the 808 nm laser (1.5 W cm$^{-2}$) for 10 min with subsequent incubation for 24 h. As seen in Fig. 4(c) and (d), **1NP** and **2aNP**-treated cells showed the predominant red fluorescence of PI and negligible green fluorescence of calcein-AM. In contrast, untreated cells and nanoparticle-treated cells

without NIR irradiation showed the prominent green fluorescence of calcein-AM and negligible red fluorescence of PI. These results suggest the significant cytotoxicity induced by the NPs *via* ROS generation upon NIR light illumination.

The quantification of cytotoxicity was performed using an MTT-based assay. This assay is used to measure the viability of cells based on the reduction of a tetrazolium-based salt (3-(4,5-dimethylthiazol-2-yl)-2,5-diphenyltetrazolium bromide or MTT) to purple formazan crystals by live and healthy cells. The viable cells contain NAD(P)H-dependent oxidoreductase enzymes, which reduce MTT to formazan, with characteristic absorption at 560 nm. The absorbance value is directly proportional to the number of viable cells. The cytotoxicity of MDA-MB-231 cells was studied independently under various conditions, as follows: (i) only NIR illumination, (ii) DSPE:mPEG$_{2000}$, (iii) nanoparticles without NIR illumination and (iv) with NIR illumination (incubated for 3 h, irradiation using 808 nm laser at 1.5 W cm$^{-2}$ for 10 min, followed by 24 h incubation) (Fig. 4(e) and (f)). Interestingly, greater cytotoxicity was observed for **1NP** and **2aNP** with NIR light illumination than for (i) NIR alone, (ii) DSPE:mPEG$_{2000}$, and (iii) nanoparticles without NIR
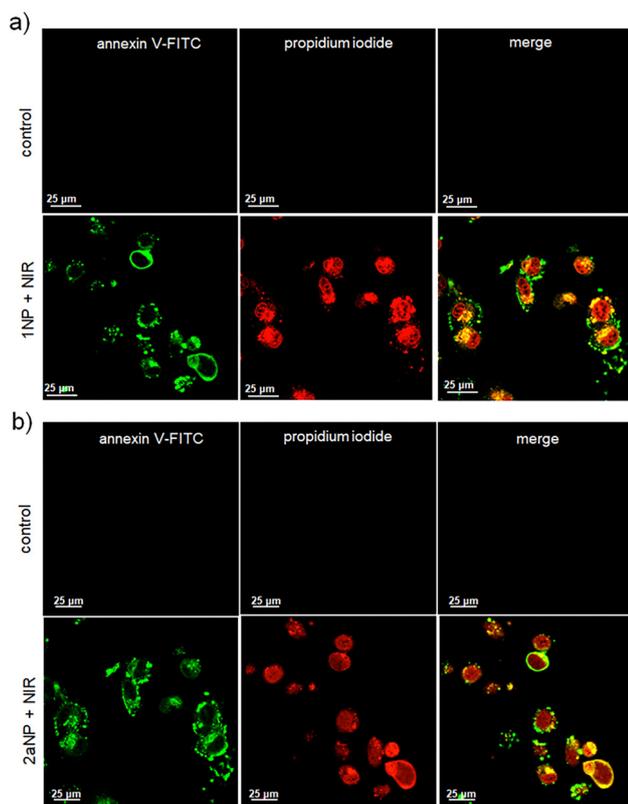
Fig. 5 Annexin V-FITC/PI assays of (a) **1NP** and (b) **2aNP**-treated MDA-MB-231 cells.

illumination. A cell death of 40% and 46% was observed for **1NP** and **2aNP**-treated cells after NIR illumination, respectively, whereas only negligible cell deaths were observed for these NPs under dark conditions. These results substantiate the importance of these macrocycle-based nanoparticles in NIR light-induced ROS generation.

To further understand the cell death mechanism of the nanoformulations, an annexin V-FITC(AV)/PI staining assay was carried out on the NP-treated MDA-MB-231 cells under NIR light illumination. Annexin V is a protein that binds to phospholipids called phosphatidylserines, which normally occur in the inner part of the cytoplasm and protrude outside only during the early stages of apoptosis. The second component is the DNA-binding dye molecule PI, which can only enter the cells when their membranes are ruptured, a characteristic of both necrosis and late apoptosis. As shown in Fig. 5, the **1NP**- and **2aNP**-treated cells exhibited the intense green fluorescence of annexin V-FITC around the cell membrane and the strong red fluorescence of PI from the nuclei upon irradiation at 808 nm laser (1.5 W cm$^{-2}$) for 10 min, followed by 24 h incubation, revealing that most of the cell population is in the late stage of the apoptotic pathway.[26]

## Conclusions

In summary, various dithienopyrrole-embedded expanded porphyrinoids were obtained by varying the number of pentafluorophenyl pendants at the *meso*-positions, and their effect on ROS generation was investigated. These newly synthesized macrocycles possessed significant absorption and emission in the NIR region, thereby targeting the well-sought optical window for therapeutics and imaging applications. Crystallographic data of **1** revealed a dome-like structure, and the electrochemical studies were in agreement with their electron-rich aromatic nature. Theoretical analysis suggested their strong aromaticity, as observed from the negative NICS values and clockwise ring currents in the AICD plots. Their photosensitizing abilities in organic media were examined using an 808 nm laser, which showed remarkable photostability and excellent ROS generation for the rubyrins bearing the maximum number of perfluorophenyl groups. These macrocycles were successfully solubilized in water using a DSPE: mPEG$_{2000}$ mixture and afforded highly photostable nanoparticles that retained the ROS generation properties. The *in vitro* experiments carried out in MDA-MB-231 cells showed good intracellular ROS generation, negligible dark cytotoxicity and significant light-induced cell death. This study also provides a wide range of possibilities in the areas of *in vivo* PDT, fluorescence imaging and $^{19}$F MRI, which have yet to be explored.

## Author contributions

A. E. performed the experimental work, DFT calculations and wrote the manuscript. T. S. helped with the synthesis and A. N. assisted with the theoretical studies. G. R. performed the *in vitro* studies and R. V. analysed the biological studies. S. G. supervised the chemistry aspects of the work.

## Conflicts of interest

There are no conflicts to declare.

## Data availability

The experimental and theoretical data supporting this article have been included as part of the SI.

The supplementary data, Cartesian coordinates for theoretical calculations and crystallographic data are provided. See DOI: **https://doi.org/10.1039/d5qm00451a**

CCDC 2380567 contains the supplementary crystallographic data for this paper.[28]

## Acknowledgements

# References

1 (a) D. E. J. G. J. Dolmans, D. Fukumura and R. K. Jain, Photodynamic Therapy for Cancer, *Nat. Rev. Cancer*, 2003, **3**, 380–387; (b) H. Abrahamse and M. R. Hamblin, New Photosensitizers for Photodynamic Therapy, *Biochem. J.*, 2016, **473**, 347–364; (c) X. Wang, J. Peng, C. Meng and F. Feng, Recent advances for enhanced photodynamic therapy: from new mechanisms to innovative strategies, *Chem. Sci.*, 2024, **15**, 12234–12257; (d) Y. Allamyradov, J. ben Yosef, B. Annamuradov, M. Ateyeh, C. Street, H. Whipple and A. O. Er, Photodynamic Therapy Review: Past, Present, Future, Opportunities and Challenges, *Photochem*, 2024, **4**, 434–461; (e) M. Li, J. Xiong, Y. Zhang, L. Yu, L. Yue, C. Yoon, Y. Kim, Y. Zhou, X. Chen, Y. Xu, X. Peng and J. S. Kim, New guidelines and definitions for type I photodynamic therapy, *Chem. Soc. Rev.*, 2025, **54**, 7025–7057.

2 M. Ethirajan, Y. Chen, P. Joshi and R. K. Pandey, The Role of Porphyrin Chemistry in Tumor Imaging and Photodynamic Therapy, *Chem. Soc. Rev.*, 2011, **40**, 340–362.

3 H. Dai, X. Wang, J. Shao, W. Wang, X. Mou and X. Dong, NIR-II Organic Nanotheranostics for Precision Oncotherapy, *Small*, 2021, **17**, 1–23.

4 (a) A. E. O'Connor, W. M. Gallagher and A. T. Byrne, Porphyrin and Nonporphyrin Photosensitizers in Oncology: Preclinical and Clinical Advances in Photodynamic Therapy, *Photochem. Photobiol.*, 2009, **85**, 1053–1074; (b) J. Kou, D. Dou and L. Yang, Porphyrin Photosensitizers in Photodynamic Therapy and Its Applications, *Oncotarget*, 2017, **8**, 81591–81603; (c) J. Tian, B. Huang, M. H. Nawaz and W. Zhang, Recent Advances of Multi-Dimensional Porphyrin-Based Functional Materials in Photodynamic Therapy, *Coord. Chem. Rev.*, 2020, **420**, 213410; (d) V. Almeida-Marrero, E. van de Winckel, E. Anaya-Plaza, T. Torres and A. de la Escosura, Porphyrinoid biohybrid materials as an emerging toolbox for biomedical light management, *Chem. Soc. Rev.*, 2018, **47**, 7369–7400; (e) P.-C. Lo, M. S. Rodríguez-Morgade, R. K. Pandey, D. K. P. Ng, T. Torres and F. Dumoulin, The unique features and promises of phthalocyanines as advanced photosensitisers for photodynamic therapy of cancer, *Chem. Soc. Rev.*, 2020, **49**, 1041–1056.

5 (a) S. Nakajima, T. Takemura and I. Sakata, Tumor-Localizing Activity of Porphyrin and Its Affinity to LDL, Transferrin, *Cancer Lett.*, 1995, **92**, 113–118; (b) J. Osterloh and M. G. H. Vicente, Mechanisms of Porphyrinoid Localization in Tumors, *J. Porphyrins Phthalocyanines*, 2002, **6**, 305–324; (c) Q. Zhang, J. He, W. Yu, Y. Li, Z. Liu, B. Zhou and Y. Liu, A Promising Anticancer Drug: A Photosensitizer Based on the Porphyrin Skeleton, *RSC Med. Chem.*, 2020, **11**, 427–437.

6 (a) M. Zhu, H. Zhang, G. Ran, D. N. Mangel, Y. Yao, R. Zhang, J. Tan, W. Zhang, J. Song, J. L. Sessler and J. L. Zhang, Metal Modulation: An Easy-to-Implement Tactic for Tuning Lanthanide Phototheranostics, *J. Am. Chem. Soc.*, 2021, **143**, 7541–7552; (b) F. Wu, Y. Sun, H. Gao, X. Zhi, Y. Zhao and Z. Shen, Boosting Near-Infrared Photothermal/Photoacoustic Conversion Performance of Anthracene-Fused Porphyrin via Paramagnetic Ion Coordination Strategy, *Sci. China: Chem.*, 2023, **66**, 164–173.

7 (a) J. L. Sessler and R. A. Miller, Texaphyrins, *Biochem. Pharmacol.*, 2000, **59**, 733–739; (b) V. Král, J. Davis, A. Andrievsky, J. Kralová, A. Synytsya, P. Poucková and J. L. Sessler, Synthesis and Biolocalization of Water-Soluble Sapphyrins, *J. Med. Chem.*, 2002, **45**, 1073–1078; (c) D. Parmeswaran, S. K. Pushpan, A. Srinivasan, M. Ravi Kumar, T. K. Chandrashekar and S. Ganesan, In Vitro and in Vivo Investigations on the Photodynamic Activity of Core-Modified Expanded Porphyrin-Ammonium Salt of 5,10,15,20-Tetrakis-(Meso-p-Sulfonato Phenyl)-25,27,29-Trithia Sapphyrin, *Photochem. Photobiol.*, 2003, **78**, 487–495; (d) L. Naumovski, M. Sirisawad, P. Lecane, J. Chen, J. Ramos, Z. Wang, C. Cortez, D. Magda, P. Thiemann, G. Boswell, D. Miles, D. G. Cho, J. L. Sessler and R. Miller, Tumor Localization and Antitumor Efficacy of Novel Sapphyrin Compounds, *Mol. Cancer Ther.*, 2006, **5**, 2798–2805; (e) Z. Wang, P. S. Lecane, P. Thiemann, Q. Fan, C. Cortez, X. Ma, D. Tonev, D. Miles, L. Naumovski, R. A. Miller, D. Magda, D. G. Cho, J. L. Sessler, B. L. Pike, S. M. Yeligar, M. W. Karaman and J. G. Hacia, Synthesis and Biologic Properties of Hydrophilic Sapphyrins, a New Class of Tumor-Selective Inhibitors of Gene Expression, *Mol. Cancer*, 2007, **6**, 9; (f) M. Ballico, V. Rapozzi, L. E. Xodo and C. Comuzzi, Metallation of Pentaphyrin with Lu(III) Dramatically Increases Reactive-Oxygen Species Production and Cell Phototoxicity, *Eur. J. Med. Chem.*, 2011, **46**, 712–720.

8 J. Tian, L. Ding, H. J. Xu, Z. Shen, H. Ju, L. Jia, L. Bao and S. Yu, Cell-Specific and pH-Activatable Rubyrin-Loaded Nanoparticles for Highly Selective near-Infrared Photodynamic Therapy against Cancer, *J. Am. Chem. Soc.*, 2013, **135**, 18850–18858.

9 (a) T. Higashino, H. Nakatsuji, R. Fukuda, H. Okamoto, H. Imai, T. Matsuda, H. Tochio, M. Shirakawa, N. V. Tkachenko, M. Hashida, T. Murakami and H. Imahori, Hexaphyrin as a Potential Theranostic Dye for Photothermal Therapy and 19F Magnetic Resonance Imaging, *ChemBioChem*, 2017, **18**, 951–959; (b) K. Hurej, W. Oszczęda, E. Opas, S. J. Zelewski, M. Pawlicki, M. J. Białek, Ł. Orzeł and L. Latos-Grażyński, Bispalladium(II) Complexes of Di-p-Pyrirubyrin Derivatives as Promising Near-Infrared Photoacoustic Dyes, *Angew. Chem., Int. Ed.*, 2023, **62**, e202303394.

10 (a) J. Ajay, T. Sulfikarali, S. M. George and S. Gokulnath, Conformationally Distinct [26]Heterorubyrin(1.1.0.1.1.0) Macrocycles and Their Bis-BODIPYs: Synthesis, Structure, and Optical Properties, *Org. Lett.*, 2022, **24**, 1000–1004; (b) A. Kalaiselvan, S. Dhamija, C. Aswathi, A. K. De and S. Gokulnath, Planar Hexaphyrin-like Macrocycles Turning into Bis-BODIPYs with Box-Shaped Structures Exhibiting Excitonic Coupling, *Chem. Commun.*, 2021, **57**, 11485–11488.

11 T. C. Pham, V. N. Nguyen, Y. Choi, S. Lee and J. Yoon, Recent Strategies to Develop Innovative Photosensitizers for Enhanced Photodynamic Therapy, *Chem. Rev.*, 2021, **121**, 13454–13619.

12 (*a*) T. Goslinski and J. Piskorz, Fluorinated Porphyrinoids and Their Biomedical Applications, *J. Photochem. Photobiol., A*, 2011, **12**, 304–321; (*b*) Y. J. Ko, K. J. Yun, M. S. Kang, J. Park, K. T. Lee, S. B. Park and J. H. Shin, Synthesis and in Vitro Photodynamic Activities of Water-Soluble Fluorinated Tetrapyridylporphyrins as Tumor Photosensitizers, *Bioorg. Med. Chem. Lett.*, 2007, **17**, 2789–2794; (*c*) N. V. S. D. K. Bhupathiraju, W. Rizvi, J. D. Batteas and C. M. Drain, Fluorinated Porphyrinoids as Efficient Platforms for New Photonic Materials, Sensors, and Therapeutics, *Org. Biomol. Chem.*, 2016, **14**, 389–408.

13 (*a*) R. A. Day and E. M. Sletten, Perfluorocarbon Nanomaterials for Photodynamic Therapy, *Curr. Opin. Colloid Interface Sci.*, 2021, **54**, 101454; (*b*) J. Králová, T. Bříza, I. Moserová, B. Dolenský, P. Vašek, P. Poučková, Z. Kejík, R. Kaplánek, P. Martásek, M. Dvořák and V. Král, Glycol Porphyrin Derivatives as Potent Photodynamic Inducers of Apoptosis in Tumor Cells, *J. Med. Chem.*, 2008, **51**, 5964–5973; (*c*) S. I. Yang, J. Seth, J. P. Strachan, S. Gentemann, D. Kim, D. Holten, J. S. Lindsey and D. F. Bocian, Ground and excited state electronic properties of halogenated tetraaryl-porphyrins. Tuning the building blocks for porphyrin-based photonic devices, *J. Porphyrins Phthalocyanines*, 1999, **3**, 117–147; (*d*) T. Korenaga, T. Shoji, K. Onoue and T. Sakai, Demonstration of the existence of intermolecular lone pair···π interaction between alcoholic oxygen and the $C_6F_5$ group in organic solvent, *Chem. Commun.*, 2009, 4678–4680; (*e*) A. M. A. Dias, C. M. B. Gonçalves, J. L. Legido, J. A. P. Coutinho and I. M. Marrucho, Solubility of oxygen in substituted perfluorocarbons, *Fluid Phase Equilib.*, 2005, **238**, 7–12; (*f*) B. W. Gung, Y. Zou, Z. Xu, J. C. Amicangelo, D. G. Irwin, S. Ma and H. C. Zhou, Quantitative Study of Interactions between Oxygen Lone Pair and Aromatic Rings: Substituent Effect and the Importance of Closeness of Contact, *J. Org. Chem.*, 2008, **73**, 689–693.

14 (*a*) D. Singh, D. Rajput and S. Kanvah, Fluorescent Probes for Targeting Endoplasmic Reticulum: Design Strategies and Their Applications, *Chem. Commun.*, 2022, **58**, 2413–2429; (*b*) J. Lin, K. Yang and E. J. New, Strategies for Organelle Targeting of Fluorescent Probes, *Org. Biomol. Chem.*, 2021, **19**, 9339–9357.

15 (*a*) M. Negi, T. Dixit and V. Venkatesh, Ligand Dictated Photosensitization of Iridium(III) Dithiocarbamate Complexes for Photodynamic Therapy, *Inorg. Chem.*, 2023, **62**, 20080–20095; (*b*) E. Zenkevich, E. Sagun, V. Knyukshto, A. Shulga, A. Mironov, O. Efremova, R. Bonnett, S. P. Songca and M. Kassem, Photophysical and Photochemical Properties of Potential Porphyrin and Chlorin Photosensitizers for PDT, *J. Photochem. Photobiol., B*, 1996, **33**, 171–180; (*c*) A. B. Marco, N. Martínez de Baroja, S. Franco, J. Garín, J. Orduna, B. Villacampa, A. Revuelto and R. Andreu,

Dithienopyrrole as a Rigid Alternative to the Bithiophene π Relay in Chromophores with Second-Order Nonlinear Optical Properties, *Chem.– Asian J.*, 2015, **10**, 188–197.

16 (*a*) M. L. Immordino, P. Brusa, S. Arpicco, B. Stella, F. Dosio and L. Cattel, Preparation, Characterization, Cytotoxicity and Pharmacokinetics of Liposomes Containing Docetaxel, *J. Controlled Release*, 2003, **91**, 417–429; (*b*) H. D. Lu, T. L. Lim, S. Javitt, A. Heinmiller and R. K. Prud'Homme, Assembly of Macrocycle Dye Derivatives into Particles for Fluorescence and Photoacoustic Applications, *ACS Comb. Sci.*, 2017, **19**, 397–406.

17 A. Edwin, G. Krishnan, A. Jayaprakash, S. Pathiyil Anilkumar and G. Sabapathi, Template Assisted Formation of 32 and 34π Octaphyrins Embedded with Dithienopyrrole Cores: A New Scaffold to Unravel Proton Coupled Redox Switching and (Anti)Aromaticity, *Chem. – Eur. J.*, 2024, **30**, e202303326.

18 (*a*) J. Min, Y. N. Luponosov, A. N. Solodukhin, N. Kausch-Busies, S. A. Ponomarenko, T. Ameri and C. J. Brabec, A Star-Shaped D-π-A Small Molecule Based on a Tris(2-Methoxyphenyl)Amine Core for Highly Efficient Solution-Processed Organic Solar Cells, *J. Mater. Chem. C*, 2014, **2**, 7614–7620; (*b*) A. Karuppusamy, R. Arulkumar, P. Kannan and P. Venuvanalingam, Effect of Increasing Methoxyphenyl Substitution on Pyrene Pyrazoline Enduring Green Light Emitting Materials, *J. Photochem. Photobiol., A*, 2019, **377**, 247–259.

19 R. Giovannetti, in *Macro To Nano Spectrosc.*, ed. J. Uddin, Intech, 2012, pp. 87–108, DOI: 10.5772/38797.

20 Y. Xiao, H. Wang, Z. Xie, M. Shen, R. Huang, Y. Miao, G. Liu, T. Yu and W. Huang, NIR TADF emitters and OLEDs: challenges, progress, and perspectives, *Chem. Sci.*, 2022, **13**, 8906–8923.

21 M. Gouterman, G. H. Wagnière and L. C. Snyder, Spectra of Porphyrins. Part II. Four Orbital Model, *J. Mol. Spectrosc.*, 1963, **11**, 108–127.

22 A. B. J. Parusel, T. Wondimagegn and A. Ghosh, Do Nonplanar Porphyrins Have Red-Shifted Electronic Spectra? A DFT/SCI Study and Reinvestigation of a Recent Proposal, *J. Am. Chem. Soc.*, 2000, **122**, 6371–6374.

23 (*a*) D. E. Hudson, D. O. Hudson, J. M. Wininger and B. D. Richardson, Penetration of Laser Light at 808 and 980 nm in Bovine Tissue Samples, *Photomed. Laser Surg.*, 2013, **31**, 163–168; (*b*) Q. Wang, J. Xu, R. Geng, J. Cai, J. Li, C. Xie, W. Tang, Q. Shen, W. Huang and Q. Fan, High Performance One-for-All Phototheranostics: NIR-II Fluorescence Imaging Guided Mitochondria-Targeting Phototherapy with a Single-Dose Injection and 808 Nm Laser Irradiation, *Biomaterials*, 2020, **231**, 119671.

24 R. Koshani and S. M. Jafari, Ultrasound-Assisted Preparation of Different Nanocarriers Loaded with Food Bioactive Ingredients, *Adv. Colloid Interface Sci.*, 2019, **270**, 123–146.

25 R. Bresolí-Obach, J. Torra, R. P. Zanocco, A. L. Zanocco and S. Nonell, in *Methods Mol. Biol.*, ed. J. Espada, Springer, US, New York, NY, 2021, pp. 165–188.

26 G. Raj, A. P. Vasantha, V. D. Sreekumar, A. V. Beena, V. K. K. Dommeti, H. Perozhy, A. T. Jose, S. Khurana and

R. Varghese, Bimetallic DNAsome Decorated with G4-DNA as a Nanozyme for Targeted and Enhanced Chemo/Chemo-dynamic Cancer Therapy, *Adv. Healthcare Mater.*, 2024, **13**, 2400256.

27 G. Raj, T. Ghosh, D. S. Vasudev, P. Harsha, D. B. Kumar, J. Prasad, V. B. Athul, S. M. Abhimanyu and R. Varghese, G4-Hemin Loaded 2D Nanosheets for Combined and Targeted Chemo-Photodynamic Cancer Therapy, *Nanoscale*, 2024, **16**, 16195–16203.

28 A. Edwin, T. Sulfikarali, G. Raj, A. Naniyil, R. Varghese and S. Gokulnath, CCDC 2380567: Experimental Crystal Structure Determination, 2025, DOI: **10.5517/ccdc.csd.cc2kx5h5**.